Improved Severe Weather Forecasts Using LEO and GEO Satellite Soundings

W. L. SMITH SR

Department of Atmospheric and Planetary Sciences, Hampton University, Hampton, Virginia, and Space Science and Engineering Center, University of Wisconsin–Madison, Madison, Wisconsin

QI ZHANG AND M. SHAO

Department of Atmospheric and Planetary Sciences, Hampton University, Hampton, Virginia

E. WEISZ

Space Science and Engineering Center, University of Wisconsin–Madison, Madison, Wisconsin

(Manuscript received 20 September 2019, in final form 26 February 2020)

ABSTRACT

It is shown here that improvements in numerical weather prediction (NWP) model forecasts of hazardous weather can be obtained by assimilating profile retrievals obtained in real time from combined direct broadcast system (DBS) polar satellite hyperspectral and geostationary satellite multispectral radiance data. Results of NWP model forecasts are shown for two recent tornado outbreak cases: 1) the 3 March 2019 tornado outbreak over the southeast United States and 2) the tornado outbreak that occurred across Illinois, Indiana, and Ohio during the night of 27 May and the morning of 28 May 2019, and 3) the 4 March 2019 severe precipitation event that occurred in southeast China. Improvements in both quantitative precipitation forecasts (QPFs) and predictions of the location of tornado occurrence are obtained. It is also shown that geostationary satellite hyperspectral soundings [i.e., *Fengyun-4A* (*FY-4A*) Geosynchronous Interferometric Infrared Sounder (GIIRS)] further improve hazardous precipitation forecasts when used, in addition to the combined polar hyperspectral and geostationary multispectral satellite profile data, to initialize the numerical forecast model. The lowest false alarm rate (FAR) and the highest probability of detection (POD) and critical success index (CSI) scores are achieved when assimilating atmospheric profile retrievals obtained by combining all the available satellite high-vertical-resolution hyperspectral radiance measurements with geostationary satellite high-spatial-resolution and high-temporal-resolution multispectral radiance measurements.

1. Introduction

Infrared radiance spectra observed with operational polar satellite hyperspectral sounding (PHS) instruments [e.g., the Infrared Atmospheric Sounding Interferometer (IASI) and the Cross-Track Infrared Sounder (CrIS)] provide relatively high-vertical-resolution temperature and moisture sounding information. This information, when received via a direct broadcast system (DBS), can be used to monitor the atmospheric stability of the atmosphere for the purpose of predicting where and when severe convective storms may develop (Smith et al. 2012; Weisz et al. 2015, 2017b). However, the temporal and horizontal resolution of the polar hyperspectral data is limited for the atmospheric stability monitoring application, being 12 h per satellite and ~15 km per footprint, depending on scan angle, respectively. Although the multispectral resolution geostationary satellite Advanced Baseline Imager (ABI) observations contain low vertical resolution water vapor and temperature sounding information, the ABI has very high temporal and horizontal resolution, the temporal resolution being 5 min and the horizontal resolution being 2 km. To facilitate the use of polar and geostationary sounding radiance information, a method for combining the PHS and ABI data has been developed to provide a satellite-sounding product with high vertical, horizontal, and temporal resolution, hereafter called "PHSnABI."

Corresponding author: Prof. William L. Smith Sr., bill.l.smithsr@gmail.com

DOI: 10.1175/JTECH-D-19-0158.1

TABLE 1. Instrument characteristics.

Instrument	IASI	CrIS	GIIRS	ABI/AHI
Satellite	*MetOp-A*, *MetOp-B*	*Suomi NPP*, *JPSS-1*	*FY-4A*	*GOES-16*
Instrument type	Michelson interferometer	Michelson interferometer	Michelson interferometer	Multispectral radiometer
Spectral resolution	0.25 cm^{-1}	0.625 cm^{-1}	0.625 cm^{-1}	34–2456 cm^{-1}
Spectral range	645–2760 cm^{-1}; 15.5–3.62 μm	650–2550 cm^{-1}; 15.4–3.9 μm	700–1130 cm^{-1}; 8.8–14.3 μm 1650–2250 cm^{-1}; 4.4–6.1 μm	751–21 277 cm^{-1}; 13.3–0.47 μm
Number of channels	8462	2211	1650	16
Spatial resolution	12 km	14 km	16 km	2 km
Launch year	2006, 2012	2011, 2017	2016	2016/14

The objectives of combining polar and geostationary sounding data are to provide improved 1) low-altitude sounding coverage across partly cloudy areas, 2) spatial details of atmospheric temperature and moisture important for high-impact weather prediction, 3) time sequences of water vapor and atmospheric stability [e.g., lifted index (LI) and convective available potential energy (CAPE)] analyses useful for nowcasting where and when convection will occur, and 4) high-spatial-resolution (2 km) and high-temporal-resolution (hourly or less) atmospheric vertical temperature and water vapor profiles to improve numerical weather prediction (NWP) model forecasts of intense weather through the quasi-continuous assimilation of the atmospheric sounding data.

The goal of this research is to demonstrate that sounding products are useful to weather service agencies for nowcasting and NWP purposes. The "nowcasting" products are produced and made available in near–real time using soundings retrieved by the fusion of direct broadcast operational polar (IASI and CrIS) hyperspectral sounding and geostationary ABI multispectral soundings (PHSnABI) derived from the radiance data. NWP products are produced by the hourly assimilation of PHSnABI soundings into a Weather Research and Forecasting (WRF) Model (Skamarock et al. 2019) configured with the same physics and forecast initialization procedures used in the NOAA Rapid Refresh Prediction (RAP) NWP model (Benjamin et al. 2016). Shao and Smith (2019) have already described the use of the WRF Model to demonstrate improved tropical storm position and precipitation forecasts using PHS data obtained during eastern U.S. landfall period of Hurricane Florence and Hurricane Michael during September and October 2018, respectively. The purpose of the forecast experiments reported here is to show the added benefit, for storm-scale forecasting, of adding available full spatial and spectral resolution all-sky condition polar satellite hyperspectral and geostationary satellite multispectral radiance data to an atmospheric background that does not include these satellite-sounding retrievals. The assimilation of sensor merged temperature and humidity profile retrievals was performed to enable the use of the entire spectrum of radiance observations, as opposed to a selection of individual channel radiances, in order to utilize the entire information content of the satellite radiance data. The condition for which there is equivalence between the assimilation of atmospheric profile retrievals and the assimilation of sensor radiances has been discussed by Migliorini (2012). Since the profile retrievals used here are derived from a linear combination of the radiances, and are vertically dealiased relative to the model background profiles (Smith et al. 2017), the result is equivalent to the assimilation of all-sky spectral radiances for all spectral channels of observation.

2. Satellite sounding instrument measurement characteristics

Table 1 shows the measurement characteristics of the polar and geostationary satellite instruments used in this study. As can be seen the spectral resolution of the hyperspectral polar satellite instruments ranges between 0.25 and 0.625 cm^{-1}, depending on instrument (i.e., IASI or CrIS), whereas the geostationary multispectral ABI instrument spectral resolution ranges from between 20 and 2456 cm^{-1}, depending on the spectral channel. However, the nadir-viewing horizontal resolution for the polar satellite hyperspectral sounders ranges between 12 and 14 km while the geostationary satellite multispectral resolution ABI is about 2 km.

3. PHS and ABI profile retrieval fusion methodology

The atmospheric profile retrieval algorithm used for PHS retrievals is the physically based dual-regression (DR) algorithm (Smith et al. 2012; Weisz et al. 2013). DR is a single field-of-view (FOV), all-sky condition, retrieval algorithm developed to provide atmospheric soundings and surface and cloud parameters from any of the operational hyperspectral sounders orbiting Earth.

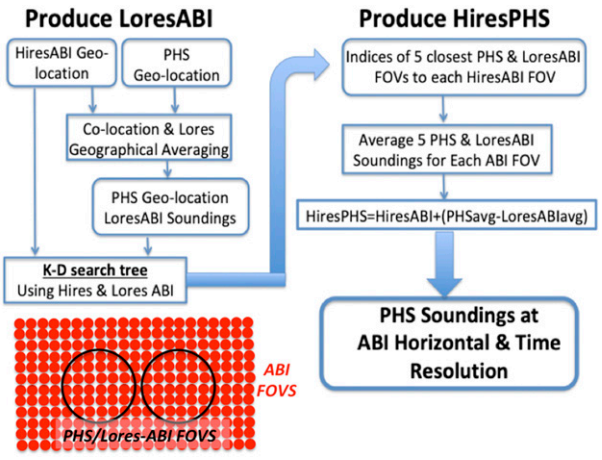

FIG. 1. Schematic diagram showing the process for combining low-vertical-resolution ABI clear-sky regression retrievals with high-vertical-resolution DRDA all-sky retrievals. A satellite footprint diagram is also shown.

The origin of the DR single FOV and all-sky multiple-regression principal component (PC) retrieval methodology dates back to the 1980s, having been used, before the advent of satellite hyperspectral instruments, to process airborne hyperspectral radiance data provided by the High-Resolution Interferometer Sounder (HIS; 1986–98), National Polar-Orbiting Operational Environmental Satellite System Airborne Sounder Test Bed–Interferometer (NAST-I; 1998 to present), and Scanning High-Resolution Interferometer Sounder (S-HIS; 1999 to present) aircraft interferometers (see Smith et al. 2009). More recently, a fast-physical method, based on applying Principal Component Radiative Transfer Model (PCRTM) (Liu et al. 2006) calculations to numerical forecast model profile data, has been implemented for eliminating the vertical resolution alias produced by the vertically smooth characteristics of the mean profile of the statistical sample used to create the regression retrievals (Smith and Weisz 2017). The vertically smoothed nature of retrieved profiles inhibits the assignment of observed radiance time and spatial variations to the exact vertical layers responsible for those variations. Thus, the vertical resolution of regression-retrieved profiles must be enhanced, using the forecast model background as a constraint in a dealiasing process. The vertically enhanced DR retrievals are hereafter called DRDA retrievals, where DA stands for the vertically dealiasing correction step in the retrieval process. The vertical dealiasing process is particularly important for NWP applications of the profile data since it results in a profile retrieval vertical resolution consistent with the vertical resolution of the model background field into which the retrievals are to be assimilated. Also, important for the NWP application of the data, the PCRTM DRDA algorithm is able to produce atmospheric soundings of temperature, water vapor, and various trace gases, together with cloud-top altitude and surface skin temperature, in real time from DBS hyperspectral sounding radiance spectra.

The ABI geostationary satellite profile retrievals are obtained using clear-sky radiance trained multiple linear regression relations based on exactly the same climatological surface and atmospheric sounding database used for the PHS DR retrieval described above (Smith et al. 2012). ABI infrared brightness temperatures for spectral channels 8–16 with center wavelengths near 6.2, 7.0, 7.3, 8.5, 9.6, 10.4, 11.2, 12.3, and 13.3 μm, respectively, are used as the predictors of surface skin temperature and the atmospheric temperature and water vapor specific humidity profiles.

Figure 1 is a schematic illustrating how PHS (i.e., CrIS, and IASI) DRDA retrievals are combined with ABI regression retrievals to form PHSnABI retrievals. Prior to the fusion process, the ABI retrievals are produced with the 5-min-interval frequency that the ABI data are being received at the University of Wisconsin–Madison (UW). A cloud mask (Heidinger et al. 2012) is used to identify the clear-sky ABI fields of view to be used in the profile fusion process. At the same time, the latest IASI or CrIS radiance data received at the UW and Hampton University (HU) DBS ground stations are transformed to vertical sounding retrievals using the DRDA algorithm. Once both the PHS and the ABI retrievals are available, they are fused together as shown in Fig. 1 and described as follows:

1) The high-horizontal-resolution ABI data (i.e., called "HiresABI") are collocated with the PHS retrievals and the "HiresABI" retrievals are averaged over the areas defined by each of the PHS fields of view (i.e., see the footprint diagram insert in Fig. 1). This provides PHS geolocated "LoresABI" soundings.
2) A nearest neighbor search engine (e.g., Bentley 1975), specifically the multidimensional (k-d) tree algorithm, is used to find the N closest LoresABI FOVs to each HiresABI pixel. It is emphasized that "closeness" is defined here in terms of temperature and moisture retrieval values at 10 levels between 100 and 1000 hPa, spaced 100-hPa apart, as well as their geographical proximity. The k-d tree algorithm is also discussed by Weisz et al. (2017a, 2019), where the search is applied on imager radiances rather than on imager sounding retrievals.
3) The most likely PHS retrieval that corresponds to each HiresABI location and time is then defined as the average of the N PHS retrievals ($N = 5$) chosen as the

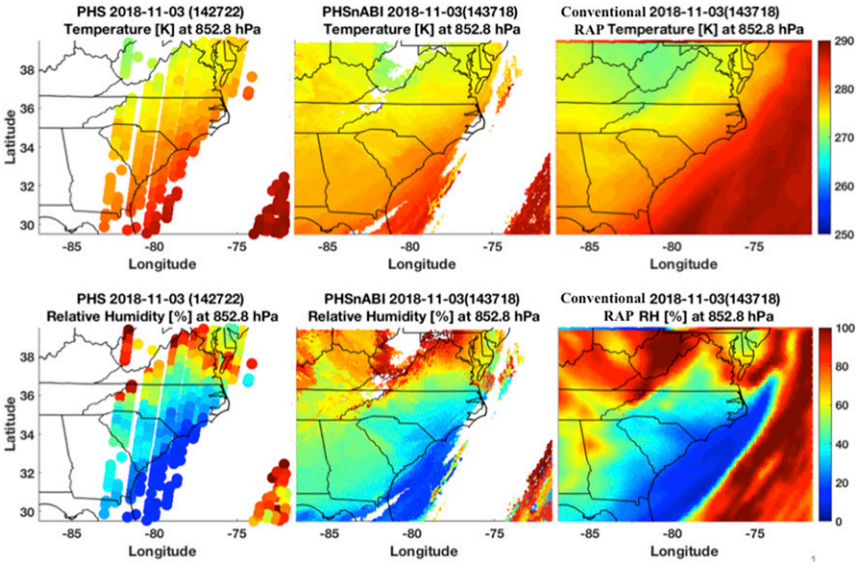

FIG. 2. (left) PHS, (center) PHSnABI, and (right) RAP temperature and relative humidity analyses for the 852.8-hPa retrieval atmospheric level.

"closest," as defined in step 2 above, to their collocated LoresABI FOV. The average of the actual LoresABI retrievals (i.e., defined as LoresABIavg), corresponding to the exact same 5 PHS FOVs, is also computed.

4) The results of step 3 are then used to predict the PHS sounding for each HiresABI sounding location and time using the equation

$$\text{HiresPHS} = \text{HiresABI} + (\text{PHSavg} - \text{LoresABIavg}), \quad (1)$$

where HiresPHS is the predicted PHS sounding at the HiresABI retrieval location and time, and PHSavg and LoresABIavg are the averages of the five "closest" PHS and LoresABI sounding retrievals as computed in step 3.

5) A forecast model dependent atmospheric temperature and moisture variable correction for the time difference between the HiresABI and the LoresABIavg/PHS observation, which is usually less than 9 h, is given by

$$\text{TC} = \text{HiresM} - \text{LoresM}, \quad (2)$$

where HiresM is the model predicted sounding variable at the HiresABI retrieval location and time, and LoresM is the average of the model predicted sounding variable at the LoresABIavg and PHS locations and times corresponding to the sounding retrievals used in step 3. The time correction is added to the HiresPHS result shown in Fig. 1.

Figure 2 shows example fusion results for the lower-troposphere 852.8-hPa retrieval level (i.e., approximately 850 hPa) over southeastern United States. As can be seen, the fusion process enables the 2-km horizontal resolution ABI data to be used to fill in the gaps of the PHS retrievals below a broken cloud cover within the PHS FOV, and beyond the edge of the polar instrument scan swath width, as well as produce PHSnABI retrievals at the full spatial and time resolution of the original ABI retrievals (i.e., 5 min and 2 km). Here, the analysis from the Rapid Refresh (RAP) NWP model is used to validate the fusion results shown. Once the results from step 3 of the fusion

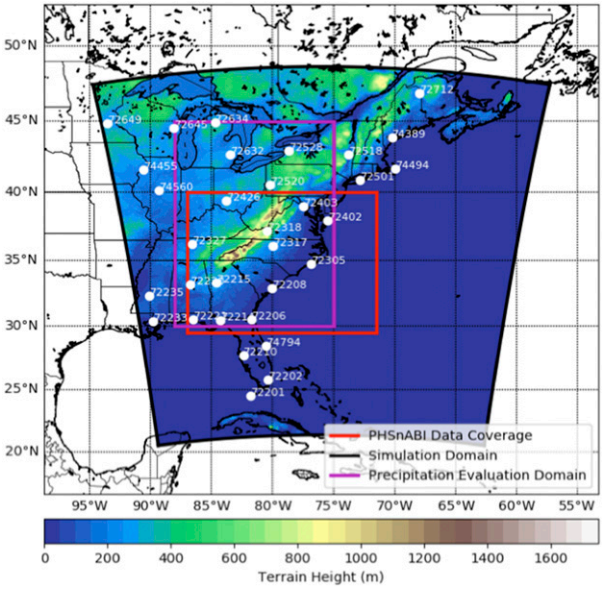

FIG. 3. Model domain, PHSnABI data coverage, and precipitation validation area used for the 3 Mar 2019 Hampton University NWP forecasts with radiosonde station IDs also shown.

TABLE 2. The experimental setup of the WRF Model used to generate forecasts by assimilating PHSnABI satellite sounding retrievals obtained on 3 Mar 2019.

		Experiment name	
		Control forecast	PHSnABI forecast
Data assimilation settings	Software	comGSIv3.6 (Shao et al. 2016)	comGSIv3.6
	Data assimilation method	3Dvar	3Dvar
Model settings	Software	WRFV4.0.2	WRFV4.0.2
	Longwave radiation	RRTMG (Iacono et al. 2008)	RRTMG
	Shortwave radiation	RRTMG	RRTMG
	Microphysics	Thompson aerosol aware (Thompson and Eidhammer 2014)	Thompson aerosol aware
	Cumulus parameterization	Grell–Freitas ensemble (Grell and Freitas 2014)	Grell–Freitas ensemble
	Surface-layer scheme	MYNN (Mellor et al. 1982)	MYNN
	Land surface scheme	Unified Noah (Chen et al. 1996)	Unified Noah
	Planetary boundary layer	MYNN 2.5-level TKE (Nakanish 2001)	MYNN 2.5-level TKE
	Soil levels	9	9
	Atmosphere vertical levels	51	51
	Model top	100 hPa	100 hPa
Data assimilation data used	Observations	Conventional observations, AMSUA, MHS, HIRS/4, radar radial wind, satellite wind	Conventional observations, PHSnABI sounding retrievals, radial wind, satellite wind
	Background error covariance	nam_glb_berror.f77.gcv	nam_glb_berror.f77.gcv
Forecast data used	Lateral boundary	GFS 0.25° forecast (BC updated at each forecast loop)	GFS 0.25°forecast (BC updated at each forecast loop)
	Initial condition	Cold start: GFS 0.25°; warm start: previous forecast	Cold start: GFS 0.25°; warm start: previous forecast

process are available, these values are used with Eq. (1) to predict PHS soundings at ABI locations and times beyond the time of the latest PHS retrievals. Once a new polar-orbit overpass becomes available, the fusion results of steps 1 and 2 are updated. In practice, the latest two polar orbits of PHS retrievals, with a sample size greater than 500 soundings each, are used in order to insure adequate coverage and representativeness of the entire ABI area considered (i.e., 28°–48°N, 70°–95°W).

4. Applications to NWP

a. The 3 March 2019 tornado outbreak

For the purpose of demonstrating the impact of the PHSnABI data on forecasting severe convective weather development, the WRF has been configured with a 9-km horizontal resolution and the RAP numerical and physical schemes used operationally. The forecast model horizontal-resolution limitation of 9 km was due primarily to the computer resources available at the time that the model was implemented to provide the results illustrated in this paper. Since that time, a computer cluster has been implemented to allow the model resolution to be increased from 9 to 3 km, which is similar to the High-Resolution Rapid Refresh (HRRR) model that is run operationally by NOAA.

Figure 3 shows the model domain and the area of PHSnABI sounding data that were assimilated on 3 March 2019, the day that a tornado outbreak occurred across the southeastern United States in which 23

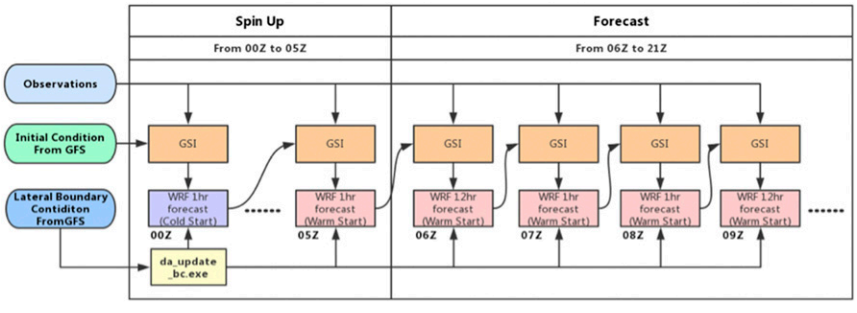

FIG. 4. Flowchart showing the hourly interval assimilation of observations.

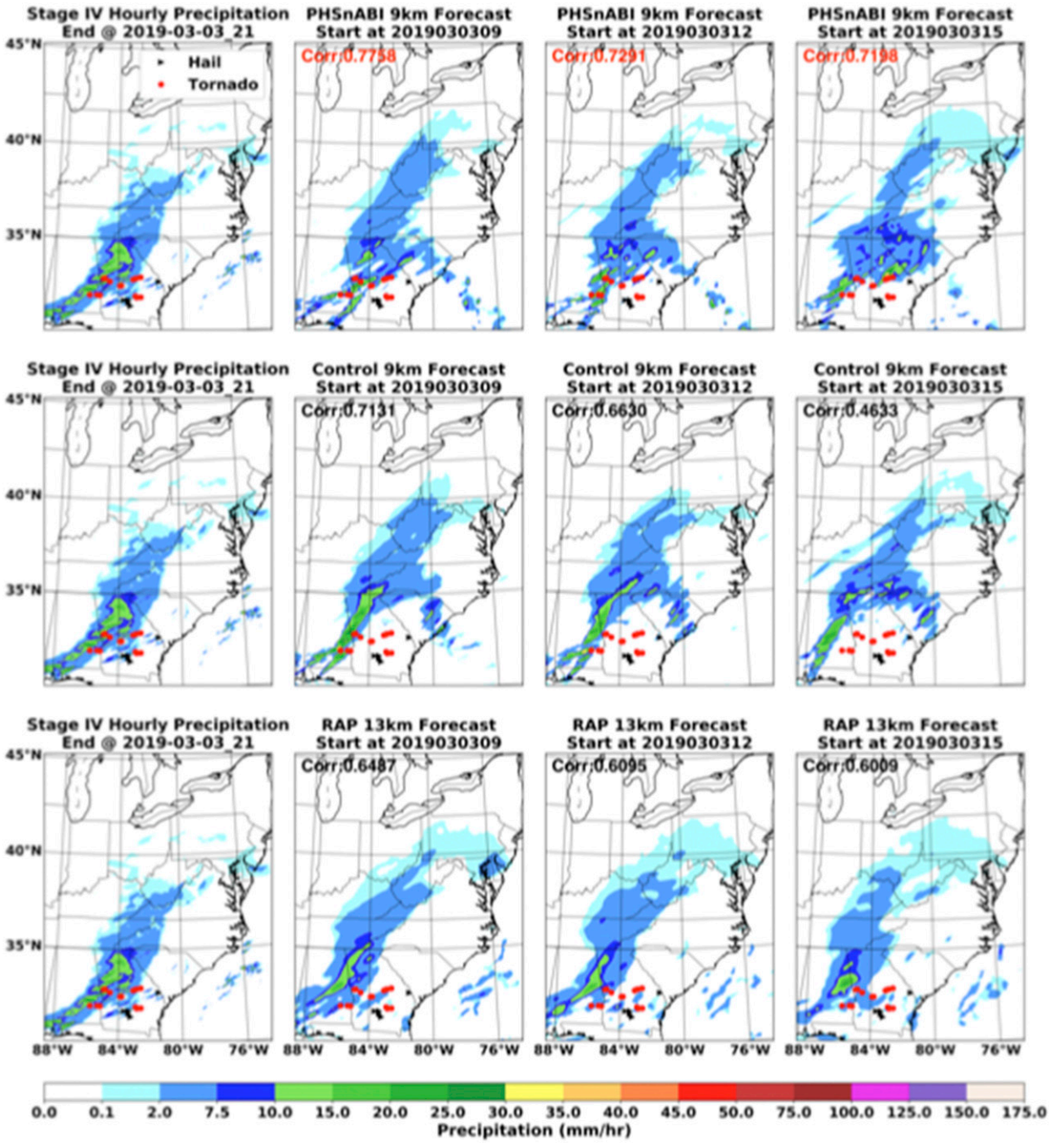

FIG. 5. NCEP Stage IV (radar and rain gauge) hourly accumulated precipitation observations and predicted precipitation from 2000 to 2100 UTC from the 12-, 9-, and 6-h control forecast and the PHSnABI forecast, initiated at 0900, 1200, and 1500 UTC, respectively. The NOAA operational RAP forecast results for exactly the same initiation times as the WRF forecasts are shown for comparison. The correlations between the forecast precipitation with the Stage IV observations are shown in each panel, with the best correlation of all three (PHSnABI, control, RAP) forecasts being displayed in red. Also shown are the tornado (red circles) and hail reports (black triangles) that were reported for the forecast period from 2000 to 2100 UTC.

lives were lost. Over the course of 6 h, a total of 41 tornadoes touched down across portions of Alabama, Georgia, Florida, and South Carolina. An EF4 tornado devastated rural communities in Alabama and Georgia killing 23 people and injuring more than 100 others.

The experimental settings of the WRF Model for the 3 March forecasts are shown in Table 2. A "control

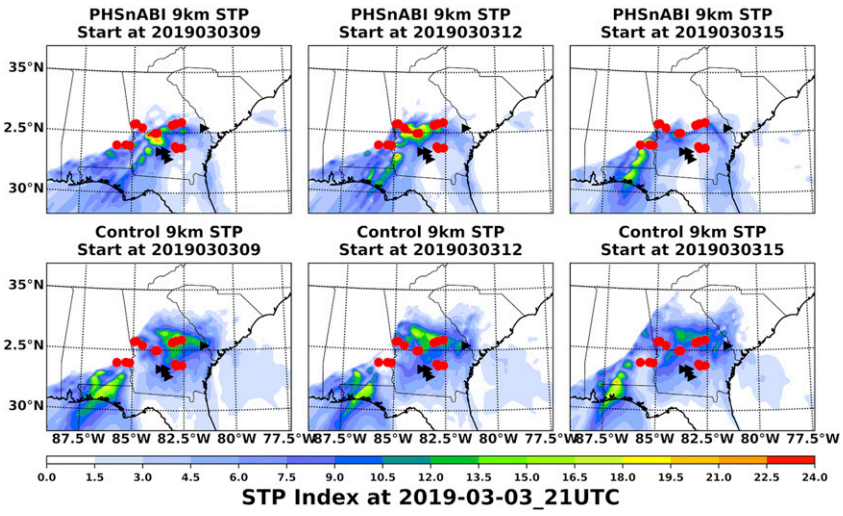

FIG. 6. The 2100 UTC (top) PHSnABI and (bottom) control forecasts for 12-, 9-, and 6-h forecast lead times, initiated at 0900, 1200, and 1500 UTC, respectively. The severe weather reports shown are for the 1-h time period of 2000–2100 UTC.

forecast,'' which used all the RAP model physics and parameterization schemes and observations used operationally, except the hyperspectral radiances assimilated in the operational RAP system, was run to compare with the ''PHSnABI forecast.'' Since the control run is configured to produce forecasts similar to those produced by NOAA's operational RAP model, the differences between the RAP and the control that result are due their spatial resolution difference (9 vs 13 km) and the assimilation of the hyperspectral radiances in the operational RAP. As shown in Table 2, the ''PHSnABI forecast'' was set up the same way as the control forecast with the exception that the PHSnABI satellite soundings were assimilated in place of the AMSU, Microwave Humidity Sounder (MHS), and High-Resolution Infrared Sounder/4 (HIRS/4) satellite radiance observations assimilated in the control forecast.

The assimilation of the conventional, radar radial wind, and satellite profile retrievals was performed on an hourly basis as shown in Fig. 4. After an initial 5-h spinup period, the observations are assimilated hourly, with 1–12-h forecasts being produced with a reinitialization frequency of 3 h (i.e., 1–12-h forecasts were produced every 3 h). Thus, using the hourly data assimilation scheme shown in Fig. 4, prior data have an influence on the current model forecast, their influence dependent on the frequency and spatial coverage of the observations being used. In the case of the PHSnABI data, the latest satellite soundings have the greatest influence because of their hourly frequency and dense area data coverage.

Figure 5 shows an example of the 11–12-, 8–9-, and 5–6-h PHSnABI and control hourly accumulation precipitation forecasts initialized at 0900, 1200, and 1500 UTC, respectively, 3 March 2019. The same forecasts produced operationally by NOAA using the RAP model are shown for comparison. As can be seen, the correlations of both the control and the RAP precipitation forecasts

TABLE 3. Contingency table.

		Observation	
		Happen	Not happen
Forecast	Happen	a	b
	Not happen	c	d

$$\text{CSI} = a/(a + b + c)$$
$$\text{POD} = a/(a + c)$$
$$\text{FAR} = b/(a + b)$$

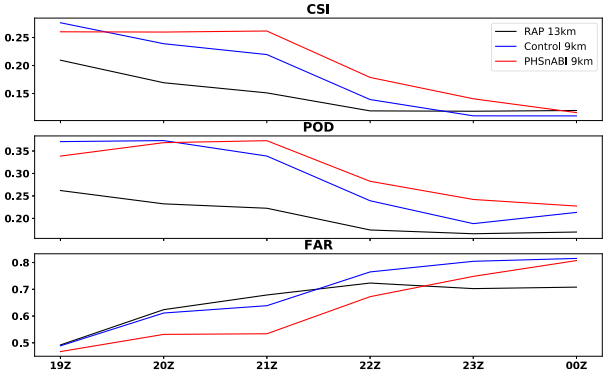

FIG. 7. Time sequence of averaged 3-, 6-, 9-, and 12-h lead-time precipitation forecast validation scores for the verification times shown at hourly intervals between 1900 UTC 3 Mar and 0000 UTC 4 Mar 2019.

are lower than the correlation of the PHSnABI forecasts with the Stage IV (Lin and Mitchell 2005) observations. Thus, the forecast using the PHSnABI data is in better agreement with observations than is the control and RAP forecasts that did not benefit from the PHSnABI observations. However, there are exceptions to this agreement such as over Georgia where the RAP forecast is superior to both the PHSnABI and the control forecasts. It can be seen that the "control" heavy precipitation forecasts conducted without the PHSnABI data are generally further away from the observed severe convection/tornado activity than it is in the PHSnABI forecasts. The "RAP" forecast precipitation across Pennsylvania that is less extensive in the PHSnABI forecast, is not verified by the Stage IV observations.

Figure 6 shows the predicted significant tornado parameter (STP), which is commonly used to forecast where tornadoes are likely to form (Saide et al. 2015; Thompson et al. 2003), at 9-, 6- and 3-h forecast lead times. Briefly the STP is a number produced as the product of the most unstable convective available potential energy (MUCAPE), effective storm-relative helicity (SRH), which measures the potential for cyclonic updraft rotation of lower (0–3 km) troposphere, the effective bulk vertical wind shear for the lower half of the storm (usually taken as the 0–6-km bulk wind difference), the lifting condensation level (LCL), and the mean parcel convective inhibition (CIN), which is the amount of energy that will prevent an air parcel from rising from the surface to the level of free convection. The formula for STP is

$$\mathrm{STP} = \frac{\mathrm{CAPE\,(J\,kg^{-1})}}{1000\,\mathrm{J\,kg^{-1}}} + \frac{\text{0–6-km wind shear}\,(\mathrm{m\,s^{-1}})}{20\,\mathrm{m\,s^{-1}}} + \frac{\mathrm{SRH\,(m^2\,s)}}{100\,\mathrm{m^2\,s}} + \frac{2000\,\mathrm{m} - \mathrm{LCL\,(m)}}{1500\,\mathrm{m}}. \quad (3)$$

As can be seen from Fig. 6, the general regions of high tornado probability are predicted relatively well by the control forecast but the area shown with high STP is relatively large, typical of the severe thunderstorm "outlook" areas provided by the Storm Prediction Center (SPC). However, the PHSnABI forecasts show greater specificity of the regions where tornadoes occurred, particularly across Georgia where the high values of PHSnABI forecast STP are generally more limited, than the control forecast STP, to where the tornadoes actually occurred (i.e., high control forecast STP values from central to northern Georgia where no tornadoes occurred. The infrared satellite retrievals are expected to improve the geographical position of highest instability through their ability to delineate the surrounding area of stable air where clouds do not obstruct the sounding of the lower troposphere.

To evaluate the performance difference between the "PHSnABI forecast," the "control forecast," the "RAP forecast," probability of detection (POD), critical success index (CSI), and false alarm ratio (FAR) scores, for hourly accumulated precipitation forecasts higher than 0.5 mm, are calculated based on the contingency table (Table 3). Averaged CSI, POD, and FAR time sequences are shown in Fig. 7, which illustrate that the "PHSnABI forecast" is a significant improvement in 0–6-h quantitative precipitation forecast performed without the satellite profile retrieval data.

The differences between the temperature and dewpoint temperature forecasts with respect to radiosonde observations (not shown) within simulation domain at 1200 UTC 3 March and 0000 UTC 4 March 2019 reveal that the "PHSnABI forecast" predicts a more accurate mid–upper-tropospheric atmospheric condition than do the "control" and "RAP" forecasts.

b. *The 27/28 May 2019 tornado outbreak*

During the evening of 27 May and into the morning of 28 May, tornadoes occurred along a path from northern Illinois, across Indiana, and into southern Ohio. Figure 8 shows the LI stability parameter derived from the PHSnABI retrievals (gap filled with RAP results) made at polar satellite overpass times and the deviation of the satellite LI values from the RAP 2-h forecast LI values, valid at the polar satellite overpass times. When the LI is negative, the atmosphere is unstable and conducive for thunderstorm development, the probability and severity depending on the LI value. The higher the magnitude of the negative LI value, the higher is the probability for severe thunderstorms to occur. It can be seen from Fig. 8, that at 1600 UTC 27 May, there was little indication of instability or thunderstorm development across the region where the tornadoes actually formed. However, by 2000 UTC, it can be seen that the atmosphere across Illinois and southwestern Indiana had become considerably unstable and this extreme instability began to spread across Indiana and into Ohio. The PHSnABI observed lifted index deviation from the 2-h RAP forecast (i.e., the lower panels for each time) suggests that the RAP forecast may have been underestimating the degree of destabilization that was taking place, particularly between 2000 UTC 27 May and 0600 UTC 28 May, the time period when most of the tornadoes occurred. It can be seen that after 0800 UTC (0300 EDT), the atmosphere once again became stable and all thunderstorm activity ceased before the time of the next polar satellite overpass time at 1400 UTC 28 May. Although not shown here, the PHSnABI soundings and derived products, such as LI, are available at hourly intervals, as well as at the polar satellite overpass times shown

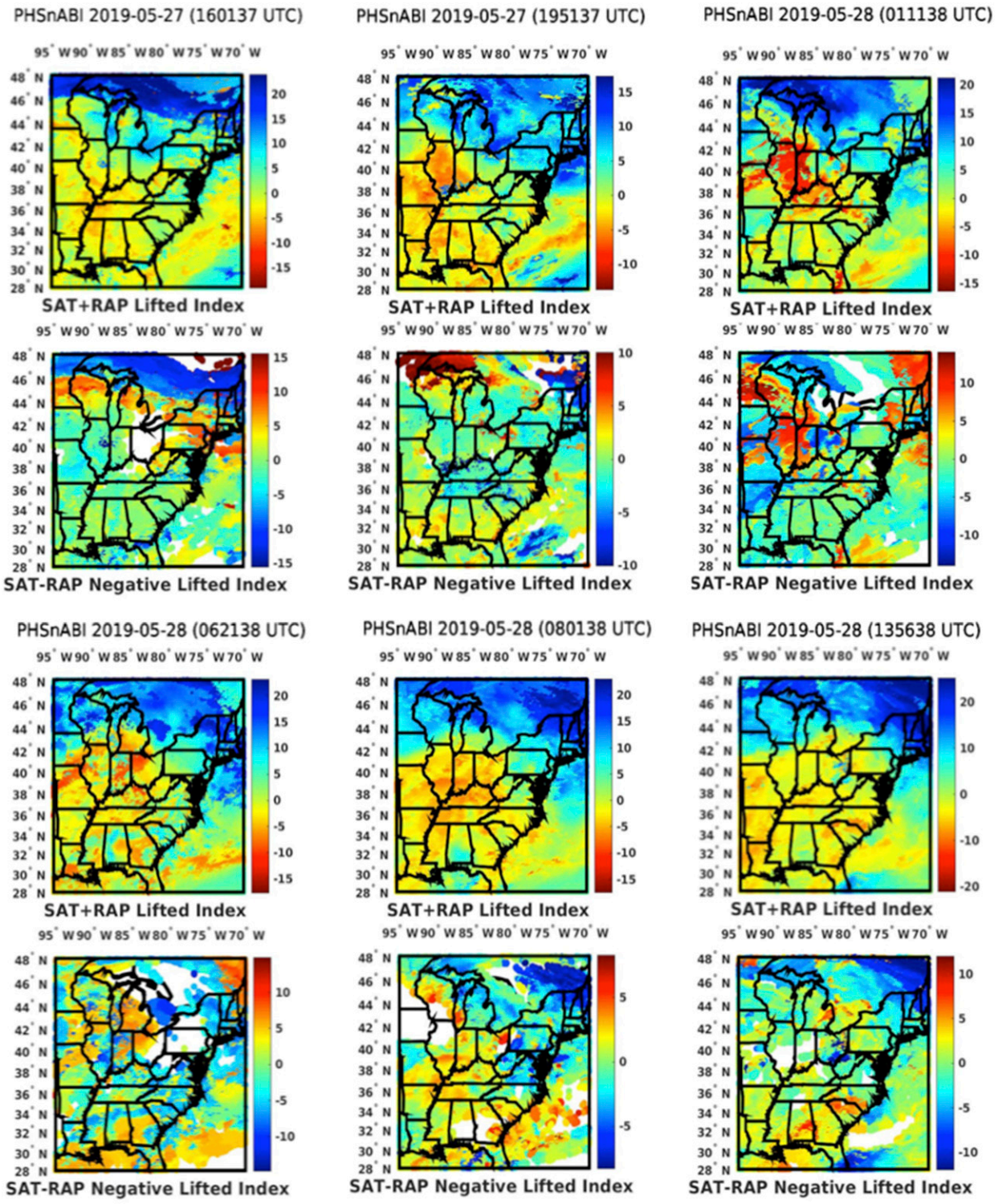

FIG. 8. (first row),(third row) The lifted index (LI) obtained by replacing RAP 2-h forecasts with satellite PHSnABI soundings where the satellite sounding retrievals are available (SAT + RAP). (second row),(fourth row) The deviation of the actual PHSnABI LI values from the RAP-2-h forecast (SAT − RAP).

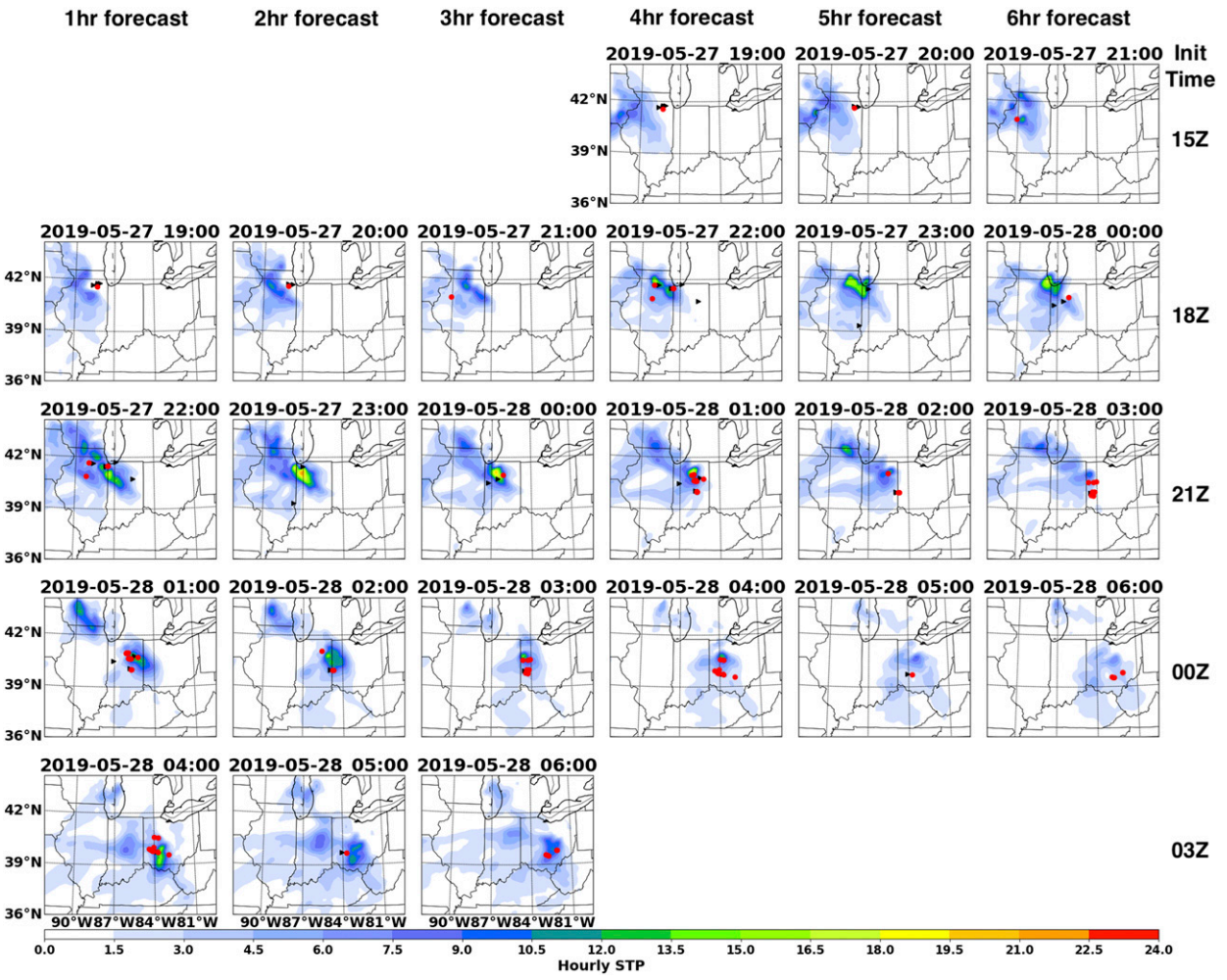

FIG. 9. STP forecasts based on the WRF Model initialized using PHSnABI soundings. Tornado and hail reports are shown by the red circles and black triangles, respectively.

here. The exact timing of the large stability changes can be best seen from the hourly interval data.

It is noted that on this day, as is now performed on a routine daily basis, the 9-km-resolution WRF Model is run for the entire geographical domain shown in Fig. 8. The hourly interval forecasts during May 2019 were made every 3 h from the hourly assimilated observations as described for the 3 March 2019 tornado outbreak case. Figure 9 shows the hourly interval forecasts of STP for the 27/28 May tornado outbreak case. As can be seen from Fig. 9, the forecast STP by the WRF Model, initialized with the PHSnABI sounding retrieval data, did predict high STP where most of the tornadoes formed for most initialization times and forecast ranges. Although there were regions of forecast moderate STP where tornadoes did not form, the model was generally successful in predicting high STP over regions where tornadoes occurred. The path along which tornadoes formed during the entire tornado outbreak period (i.e., 1800 UTC 27 May to 0600 UTC 28 May) seems to be associated with the eastern edge of he PHSnABI forecast high STP values. This is particularly evident in the forecast results shown in Fig. 9 initialized at 2100, 0000, and 0300 UTC.

Figures 10a and 10b show the precipitation forecasts for the tornado outbreak period compared to Stage IV precipitation (i.e., combined surface and radar observations) and the operational RAP precipitation forecasts. As can be seen from these comparisons, although the WRF PHSnABI forecasts are far from perfect, they are generally as good as, and often better, than those forecasts produced with the operational RAP model devoid of the PHSnABI sounding retrieval input.

The results for these two tornado outbreaks shown here are encouraging. Assuming that these results will be repeated for future tornado outbreak situations, the use of PHSnABI retrievals in mesoscale numerical models, such as

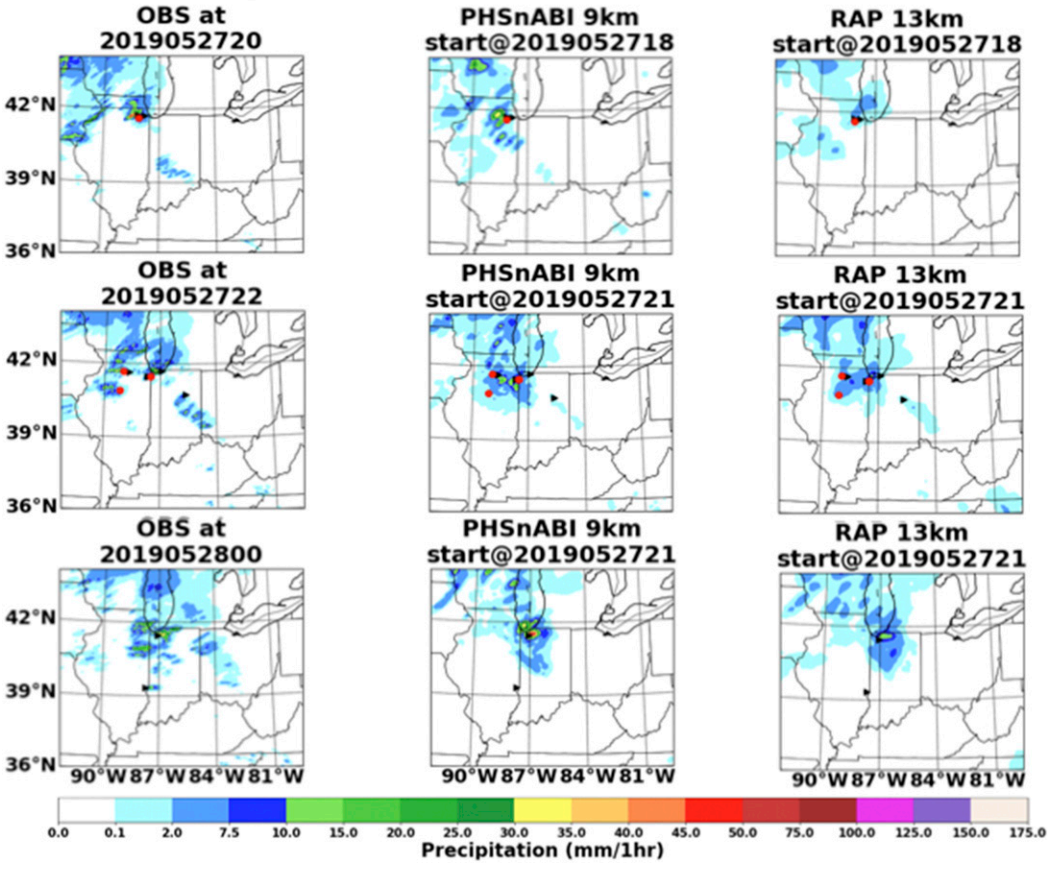

FIG. 10a. Hourly accumulated precipitation forecast for the period from 1900 UTC 27 May to 0000 UTC 28 May 2019 for both the WRF Model, which included PHSnABI data (i.e., PHSnABI forecast), and for NOAA's operational RAP model run devoid of the PHSnABI data. Tornado and hail reports are shown by the red circles and black triangles, respectively.

the NOAA RAP model, could provide a significant step forward in providing the warning time needed to save the lives of, and prevent injury to, people where tornadoes form. Of course, because the fusion process used to generate soundings with high spatial and temporal resolution from the combination of polar satellite hyperspectral and geostationary satellite multispectral radiance data is imperfect, particularly when the space and time difference between the two observations is relatively large for the mesoscale meteorological phenomena being observed, a real geostationary satellite hyperspectral sounding instrument is urgently needed to improve the reliability of potentially life-saving forecasts of severe weather, including tornadoes.

c. *The 4 March 2019 severe precipitation in Southern China*

From 0900 to 2100 UTC 4 March 2019, severe precipitation occurred in Southern China (domain is configured as shown in Fig. 11). During this period, more than 20 stations' accumulated precipitation exceeded 150 mm and multiple warnings of debris flow and landslides were triggered. With the aim of investigating the potential advantage of using of using hyperspectral soundings from geostationary satellites, the PHS and the Advanced Himawari Imager (AHI) on board the *Himawari-8* satellite, along with the Geosynchronous Interferometric Infrared Sounder (GIIRS) on board the *Fengyun-4* (*FY-4*) satellite are used for conducting a heavy precipitation forecast case study. The AHI radiance data were used in place of those derived from the ABI data to produce the combined hyperspectral and multispectral temperature and water vapor soundings for this region. It is important to note that the original level-1 GIIRS radiance data possessed both spectral and radiometric calibration deficiencies resulting from the initial calibration procedures used. However, the spectral calibration errors were corrected at the University of Wisconsin–Madison through a recalibration process (R. Knuteson 2019, personal communication) prior to the sounding retrieval process. Significant radiometric calibration errors in the GIIRS

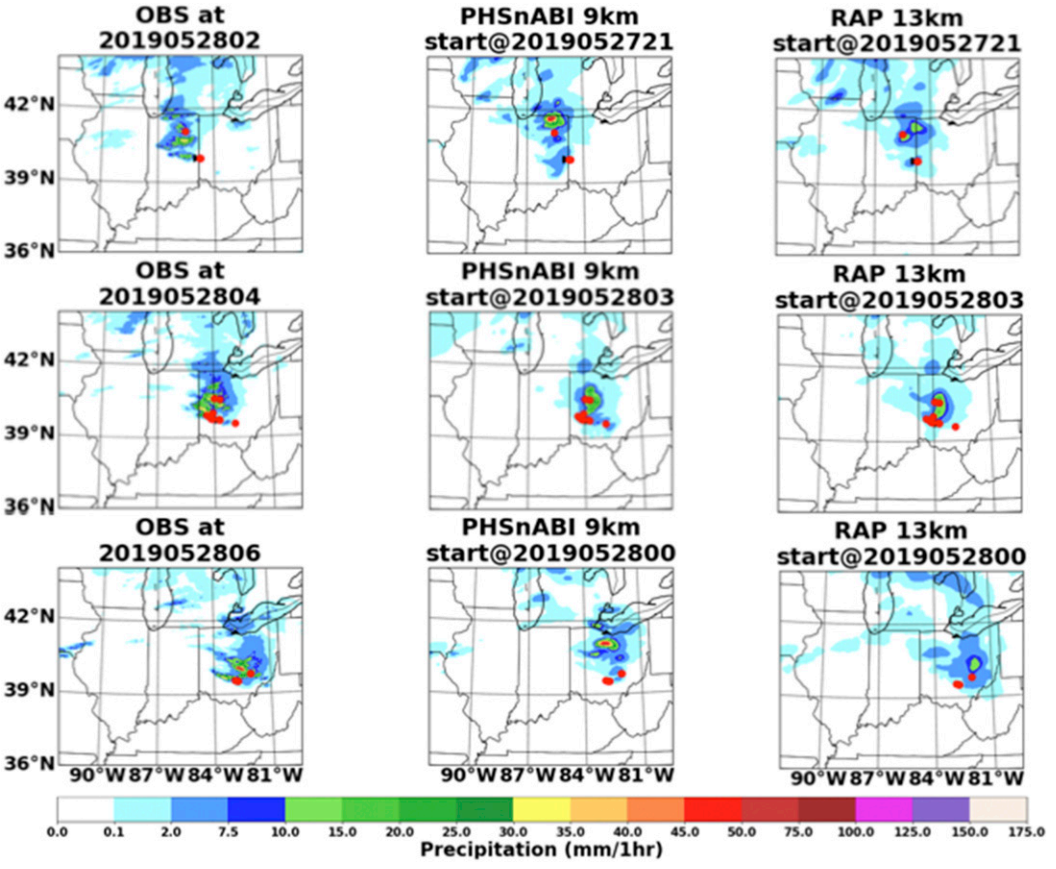

FIG. 10b. As in (a), but for the period from 0100 to 0600 UTC 28 May 2019.

radiance spectra were detected through spectral radiance feature comparisons with spectral features of radiance spectra calculated using the forecast model background atmospheric profiles. Inconsistent spectral features were assumed to indicate poorly calibrated GIIRS radiance spectra and these spectra were excluded from the sounding retrieval process.

Figure 12 shows us the 3-hourly accumulated precipitation defined using the CPC morphing technique (CMORPH) (Joyce et al. 2007) for the production of global precipitation estimates and the forecast results obtained by assimilating the PHSnAHI, PGSnAHI, and GHSnAHI data as well as for the control experiment and the results obtained from the China Meteorological Administration's Global/Regional Assimilation And Prediction System's Mesoscale (GRAPES-MESO) weather forecast system (Long-Ke et al. 2011). It can be easily seen that PHSnAHI and PGSnAHI forecasts show much better spatial correlation coefficients compared to the control and the GRAPES-MESO results when heavier precipitation occurred.

The 3-hourly accumulated heavy precipitation (i.e., precipitation $>$ 7.5 mm) CSI, POD, and FAR scores for the various model runs are shown in Fig. 13. Positive impact of the inclusion of the GIIRS data on NWP system is clearly seen. Overall, the lowest FAR, highest POD and CSI are all achieved when the assimilated

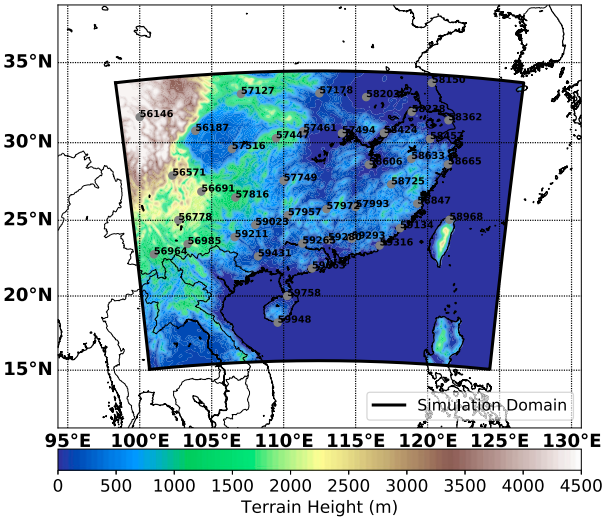

FIG. 11. Model domain for the 4 Mar 2019 southern China case. Radiosonde station locations and identifiers are overlain.

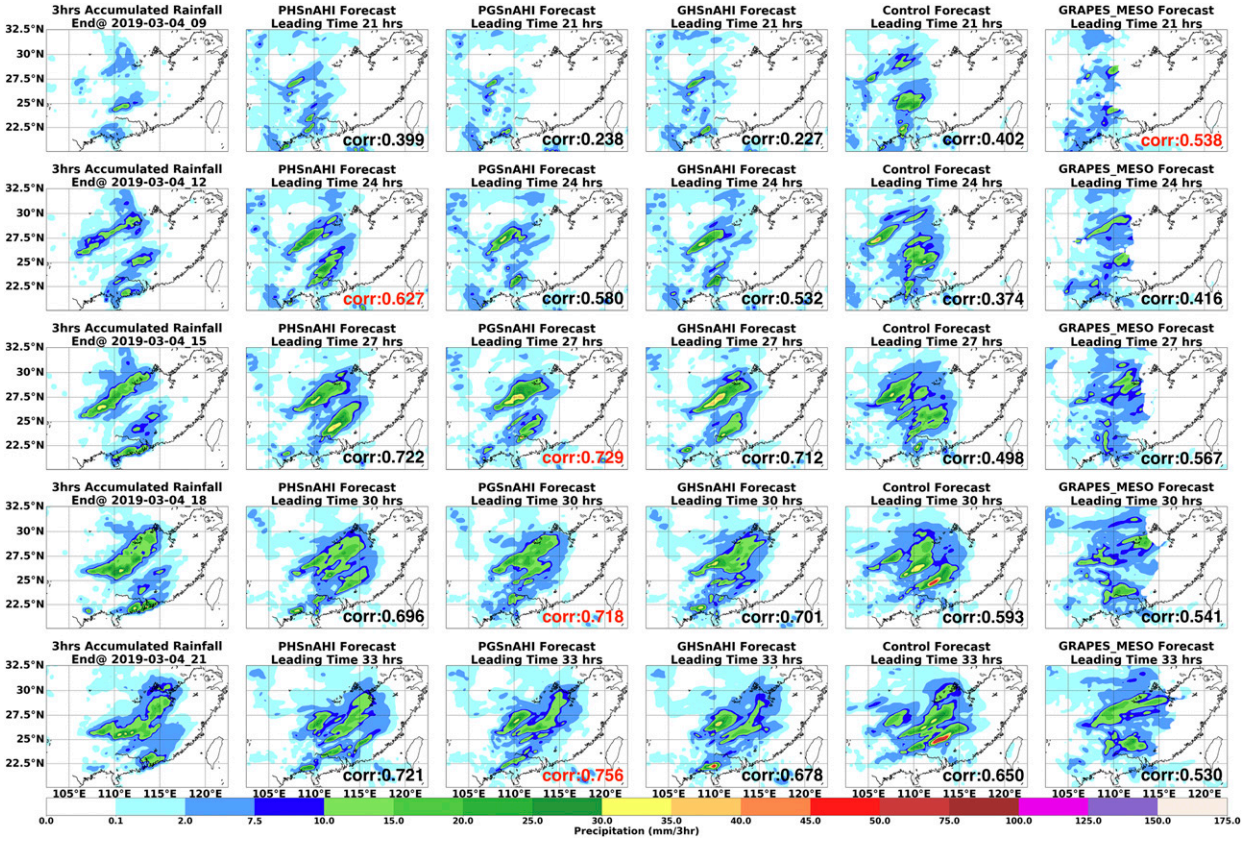

FIG. 12. (left) The 3-hourly accumulated CMORPH (satellite and rain gauge) merged 10-km gridded precipitation from 0900 to 2100 UTC compared to (remaining columns) the ''PHSnAHI,'' ''PGSnAHI,'' ''GHSnAHI,'' ''control,'' and ''GRAPES-MESO'' 3-hourly precipitation accumulation forecasts initialized at 0900 UTC 3 Mar 2019. The correlations between the forecast precipitation with the CMORPH ''observations'' are shown in each panel, with the best correlation of all five forecasts being displayed in red.

atmospheric retrievals are defined by using both GEO and LEO hyperspectral radiances with multispectral radiances from AHI (i.e., PGSnAHI). Moreover, the bias and standard deviation of the initial temperature and water vapor profiles are largely reduced when the PHSnAHI and PGSnAHI data are assimilated (Fig. 14). It can also be seen that the GHSnAHI retrieval accuracy is inferior to the PHSnAHI retrieval accuracy due to the fact that the CrIS and IASI radiometric calibration was more accurate than that for the GIIRS data used in this study. However, the residual radiometric calibration errors in the GIIRS data have been identified and the radiometric calibration algorithm is being improved for application to future GIIRS interferometer measurements.

5. Summary and conclusions

Direct broadcast satellite (DBS) polar satellite hyperspectral soundings can be combined with geostationary satellite multispectral soundings to provide in real time high-spatial-resolution and high-temporal-resolution atmospheric sounding products. These products can be used to improve the prediction of the timing and the general location of intense convection and associated severe storms. In particular, the combined polar and geostationary sounding products 1) improve low-altitude sounding coverage across partly cloudy areas, 2) observe spatial details of atmospheric temperature and moisture important for severe weather prediction, 3) provide high temporal resolution and critical information as needed to predict the time of the onset of severe convection. A WRF Model configured in a manner similar to NOAA's operational RAP is being run daily at Hampton University, 24/7, producing 0–12-h forecast every hour. Results obtained for two recent significant tornado outbreak cases indicate the potential value of the high-spatial-resolution and high-temporal-resolution satellite sounding data to improve convective weather forecasts, including the general location of heavy precipitation and tornadoes.

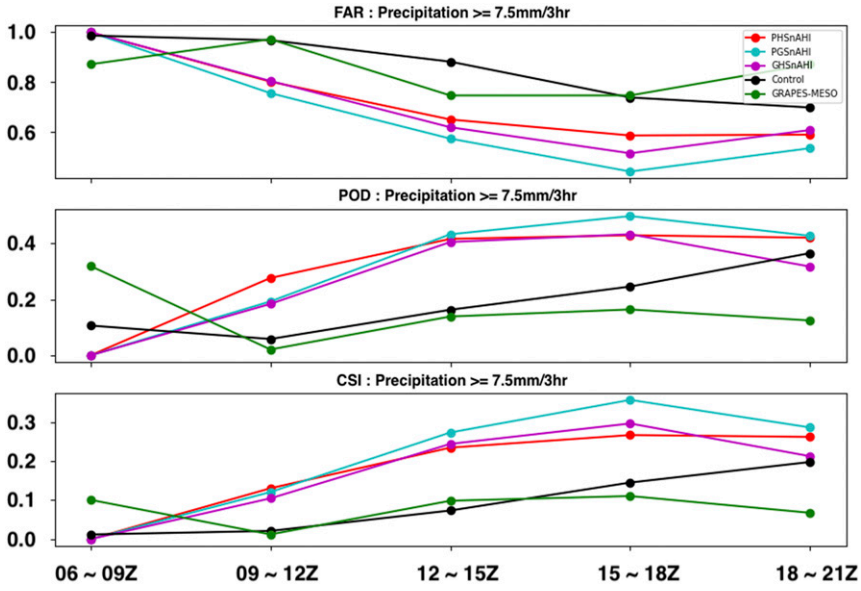

FIG. 13. The 3-hourly accumulated heavy precipitation false alarm ratio (FAR), probability of detection (POD), and critical success index (CSI) associated with various forecast runs shown in Fig. 12 using different initial datasets.

It is important to note that we cannot generalize the improvements for the three cases shown here to all weather situations. For this reason, the forecast model described here is now being run every day, on an hourly basis, in order to obtain a statistically significant number of forecasts covering the entire range of atmospheric conditions observed over an entire year. Only after such a large and representative sample of atmospheric conditions is obtained, will it be possible to state that the high-resolution satellite data provide consistent significant improvements in the skill for predicting convective weather events. Moreover, although not perfect, if results like, those presented here, continue to be demonstrated through real-time applications of these data, operational agencies, such as NOAA, might start using these satellite-sounding retrievals to improve their operational severe weather predictions. Such improvements could result in the saving of lives and the prevention of injury by significantly increasing the severe weather warning lead time to that needed for preparing for such catastrophic weather events.

Finally, it is shown for a severe precipitation event in China, that geostationary satellite–hyperspectral sounding data can further improve severe weather numerical forecasts. This improvement results from the provision of hyperspectral resolution vertical soundings, rather than solely multispectral resolution soundings, within the space and time gaps of the polar hyperspectral data. Future improvements in the calibration of the *FY-4A* GIIRS data are expected to produce much more dramatic improvements, than those shown here, through the incorporation of the geostationary hyperspectral sounding (GHS) data. Eventually, improvements in global hazardous weather predictions

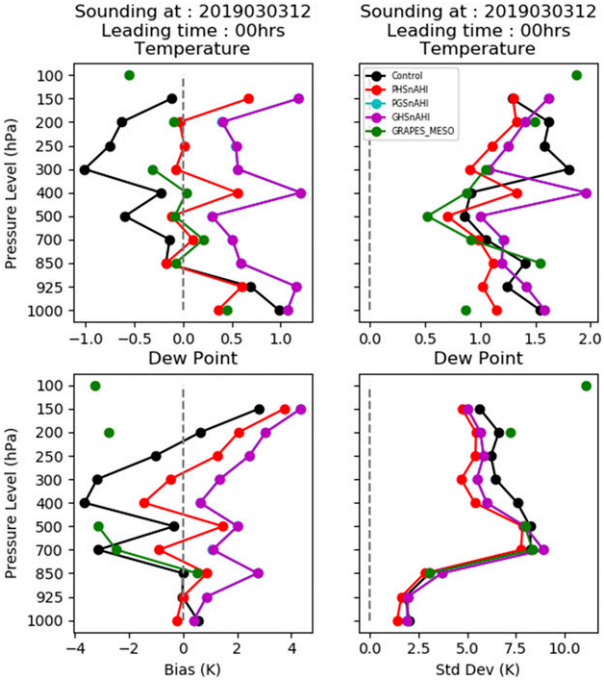

FIG. 14. Bias and standard deviation of the differences between profile temperature and dewpoint data and radiosonde temperature and dewpoint observations within the forecast domain shown in Fig. 11.

can be expected when high-spatial-resolution and high-temporal-resolution hyperspectral sounding instruments are carried on the future international system of geostationary satellites.

Acknowledgments. The authors would like to acknowledge the financial support provided by the NOAA JPSS Program Office Proving Ground and Risk Reduction (PGRR) project under Grant NA15NES4320001 and the NASA MUREP Institutional Research Opportunity (MURO) program under Grant NX15AQ03A. The administrative support of Dr. Mitch Goldberg (NOAA), and Drs. James Russell, M. Patrick McCormick, and William Moore (Hampton University), as well as Mr. Wayne Feltz (University of Wisconsin–Madison), is greatly appreciated. The authors acknowledge the technical support provided by Dr. John McNabb and Mr. Anthony DiNorscia at the Hampton University and Mr. Erik Olson and Drs. Liam Gumley, Jordan Gerth, and Scott Lindstrom at the University of Wisconsin–Madison.

REFERENCES

Benjamin, S. G., and Coauthors, 2016: A North American hourly assimilation and model forecast cycle: The Rapid Refresh. *Mon. Wea. Rev.*, **144**, 1669–1694, https://doi.org/10.1175/MWR-D-15-0242.1.

Bentley, J. L., 1975: Multidimensional binary search trees used for associative searching. *Commun. ACM*, **18**, 509–517, https://doi.org/10.1145/361002.361007.

Chen, F., and Coauthors, 1996: Modeling of land surface evaporation by four schemes and comparison with FIFE observations. *J. Geophys. Res.*, **101**, 7251–7268, https://doi.org/10.1029/95JD02165.

Grell, G. A., and S. R. Freitas, 2014: A scale and aerosol aware stochastic convective parameterization for weather and air quality modeling. *Atmos. Chem. Phys.*, **14**, 5233–5250, https://doi.org/10.5194/acp-14-5233-2014.

Heidinger, A. K., A. T. Evan, M. J. Foster, and A. Walther, 2012: A naive Bayesian cloud-detection scheme derived from *CALIPSO* and applied within PATMOS-x. *J. Appl. Meteor. Climatol.*, **51**, 1129–1144, https://doi.org/10.1175/JAMC-D-11-02.1.

Iacono, M. J., J. S. Delamere, E. J. Mlawer, M. W. Shephard, S. A. Clough, and W. Collins, 2008: Radiative forcing by long-lived greenhouse gases: Calculations with the AER radiative transfer models. *J. Geophys. Res.*, **113**, D13103, https://doi.org/10.1029/2008JD009944.

Joyce, R. J., J. E. Janowiak, P. Xie, and P. A. Arkin, 2007: CPC morphing technique (CMORPH). *Measuring Precipitation from Space: EURAINSAT and the Future*, V. Levizzani et al., Eds., Advances in Global Change Research, Vol. 28, Springer, 307–317.

Lin, Y., and K. E. Mitchell, 2005: The NCEP Stage II/IV hourly precipitation analyses: Development and applications. *19th Conf. on Hydrology*, San Diego, CA, Amer. Meteor. Soc., 1.2, https://ams.confex.com/ams/Annual2005/techprogram/paper_83847.htm.

Liu, X., W. L. Smith, D. K. Zhou, and A. Larar, 2006: Principal component-based radiative transfer forward model for hyperspectral sensors. *Appl. Opt.*, **45**, 201–209, https://doi.org/10.1364/AO.45.000201.

Long, K., C. Jing, X. Ma, and Y. Ji, 2011: The preliminary study on ensemble prediction of GRAPES-meso based on ETKF[J] (in Chinese). *J. Chengdu Univ. Inf. Tech.*, **26**, 37–46.

Mellor, G. L., C. R. Mechoso, and E. Keto, 1982: A diagnostic calculation of the general circulation of the Atlantic Ocean. *Deep-Sea Res.*, **29A**, 1171–1192, https://doi.org/10.1016/0198-0149(82)90088-7.

Migliorini, S., 2012: On the equivalence between radiance and retrieval assimilation. *Mon. Wea. Rev.*, **140**, 258–265, https://doi.org/10.1175/MWR-D-10-05047.1.

Nakanish, M., 2001: Improvement of Mellor-Yamada turbulence closure model based on large-eddy simulation data. *Bound.-Layer Meteor.*, **99**, 349–378, https://doi.org/10.1023/A:1018915827400.

Saide, P. E., and Coauthors, 2015: Central American biomass burning smoke can increase tornado severity in the U.S. *Geophys. Res. Lett.*, **42**, 956–965, https://doi.org/10.1002/2014GL062826.

Shao, H., and Coauthors, 2016: Bridging research to operations transitions: Status and plans of community GSI. *Bull. Amer. Meteor. Soc.*, **97**, 1427–1440, https://doi.org/10.1175/BAMS-D-13-00245.1.

Shao, M., and W. L. Smith, 2019: Impact of atmospheric retrievals on Hurricane Florence/Michael forecasts in a regional NWP model. *J. Geophys. Res. Atmos.*, **124**, 8544–8562, https://doi.org/10.1029/2019JD030360.

Skamarock, W. C., and Coauthors, 2019: A description of the Advanced Research WRF version 4. NCAR Tech. Note NCAR/TN-556+STR, 145 pp., https://doi.org/10.5065/D6DZ069T.

Smith, W. L., Sr., and E. Weisz, 2017: Dual-regression approach for high-spatial-resolution infrared soundings. *Comprehensive Remote Sensing*, M. Goldberg, Ed., Elsevier, 297–311.

——, and Coauthors, 2009: Evolution, current capabilities, and future advances in satellite ultra-spectral IR sounding. *Atmos. Chem. Phys.*, **9**, 6541–6569, https://doi.org/10.5194/acpd-9-6541-2009.

——, E. Weisz, S. Kireev, D. K. Zhou, Z. Li, and E. E. Borbas, 2012: Dual-regression retrieval algorithm for real-time processing of satellite ultraspectral radiances. *J. Appl. Meteor. Climatol.*, **51**, 1455–1476, https://doi.org/10.1175/JAMC-D-11-0173.1.

——, ——, J. Gerth, A. DiNorscia, J. McNabb, M. Shao, M. Dutter, and J. Gagan, 2019: Developing meteorological forecast products in near real-time from hyperspectral sounder radiances. *99th Annual Meeting,* Phoenix, AZ, Amer. Meteor. Soc., 6A.1, https://ams.confex.com/ams/2019Annual/webprogram/Paper353934.html.

Thompson, G., and T. Eidhammer, 2014: A study of aerosol impacts on clouds and precipitation development in a large winter cyclone. *J. Atmos. Sci.*, **71**, 3636–3658, https://doi.org/10.1175/JAS-D-13-0305.1.

Thompson, R. L., R. Edwards, J. A. Hart, K. L. Elmore, and P. Markowski, 2003: Close proximity soundings within supercell environments obtained from the Rapid Update Cycle. *Wea. Forecasting*, **18**, 1243–1261, https://doi.org/10.1175/1520-0434(2003)018<1243:CPSWSE>2.0.CO;2.

Weisz, E., and W. P. Menzel, 2019: Imager and sounder data fusion to generate sounder retrieval products at an improved spatial and temporal resolution. *J. Appl. Remote Sens.*, **13**, 034506, https://doi.org/10.1117/1.JRS.13.034506.

——, W. L. Smith Sr., and N. Smith, 2013: Advances in simultaneous atmospheric profile and cloud parameter regression based retrieval from high-spectral resolution radiance measurements. *J. Geophys. Res. Atmos.*, **118**, 6433–6443, https://doi.org/10.1002/jgrd.50521.

——, N. Smith, and W. L. Smith Sr., 2015: The use of hyperspectral sounding information to monitor atmospheric tendencies leading to severe local storms. *Earth Space Sci.*, **2**, 369–377, https://doi.org/10.1002/2015EA000122.

——, B. Baum, and W. P. Menzel, 2017a: Fusion of satellite-based imager and sounder data to construct supplementary high spatial resolution narrowband IR radiances. *J. Appl. Remote Sens.*, **11**, 036022, https://doi.org/10.1117/1.JRS.11.036022.

——, W. L. Smith Sr., K. Strabala, A. Huang, and N. Smith, 2017b: Hyperspectral sounder derived severe weather indices. *Proc. 21st Int. TOVS Study Conf.*, Darmstadt, Germany, International TOVS Working Group, http://cimss.ssec.wisc.edu/itwg/itsc/itsc21/proceedings/11p.05_weisz.pdf.